

The impact of Faraday effects on polarized black hole images of Sagittarius A*.

Alejandra Jiménez-Rosales[★] and Jason Dexter[†]

Max-Planck-Institut für Extraterrestrische Physik, Giessenbachstr. 1, 85748 Garching, Germany

Accepted XXX. Received YYY; in original form ZZZ

ABSTRACT

We study model images and polarization maps of Sagittarius A* at 230 GHz. We post-process GRMHD simulations and perform a fully relativistic radiative transfer calculation of the emitted synchrotron radiation to obtain polarized images for a range of mass accretion rates and electron temperatures. At low accretion rates, the polarization map traces the underlying toroidal magnetic field geometry. At high accretion rates, we find that Faraday rotation internal to the emission region can depolarize and scramble the map. We measure the net linear polarization fraction and find that high accretion rate “jet-disc” models are heavily depolarized and are therefore disfavoured. We show how Event Horizon Telescope measurements of the polarized “correlation length” over the image provide a model-independent upper limit on the strength of these Faraday effects, and constrain plasma properties like the electron temperature and magnetic field strength.

Key words: accretion – black hole physics – Galaxy: centre – MHD – polarization – radiative transfer

1 INTRODUCTION

The compact radio source Sagittarius A* (Sgr A*) is the closest supermassive black hole candidate to Earth (e.g., Genzel et al. 2010; Falcke & Markoff 2013). With a mass $M \sim 4.3 \times 10^6$ solar masses and at a distance $D \sim 8.3$ kpc (Boehle et al. 2016; Gillessen et al. 2017), Sgr A* is the black hole with the largest apparent angular size on the sky (with a shadow of $\sim 50 \mu\text{as}^1$), which makes it an excellent laboratory for studying accretion physics around black holes and for probing general relativistic effects. Sgr A* emits most of its luminosity from synchrotron radiation in what is called the “submillimetre bump.” At these wavelengths ($\lesssim 1$ mm), the radiation is expected to be optically thin and originate from close to the black hole (Falcke & Markoff 2000; Bower et al. 2015).

Models of radiatively inefficient accretion flows (RIAFs Narayan & Yi 1995; Quataert & Narayan 1999; Yuan et al. 2003) and magnetised jets (Falcke & Markoff 2000; Yuan et al. 2002) have been developed to explain the radio spectrum of Sgr A*. Such models can now be realised using general relativistic magnetohydrodynamic (GRMHD) simula-

tions, which capture the time-dependent accretion process as a result of the magnetorotational instability (MRI, Balbus & Hawley 1991) including all relativistic effects. This is particularly important for interpreting mm-VLBI data from the Event Horizon Telescope (EHT), which now resolves the emission at 230 GHz on event horizon scales. The compact size found for Sgr A* is ≈ 4 Schwarzschild radii (Doeleman et al. 2008; Fish et al. 2011).

Total intensity images of submm synchrotron emission from such models predict somewhat different morphologies (size, degree of asymmetry) due to differences in the initial conditions, such as magnetic field configuration, electron-proton coupling, electron temperature distribution function and evolution, to name a few. Although any particular model is well constrained (e.g., Dexter et al. 2010; Broderick et al. 2011), the images are often dominated by the relativistic effects of light bending and Doppler beaming due to an emission radius close to the event horizon, resulting in a characteristic crescent shape (e.g., Bromley et al. 2001; Broderick & Loeb 2006; Mościbrodzka et al. 2009; Dexter et al. 2010; Kamruddin & Dexter 2013; Mościbrodzka et al. 2014; Chan et al. 2015; Ressler et al. 2017). As a result, model-dependence in parameter estimation from total intensity images is a major current issue.

The discovery of 5–10% linear polarization from Sgr A* at 230 GHz (Aitken et al. 2000) showed that the accretion rate is much less than that inferred from X-ray observa-

[★] E-mail: ajimenez@mpe.mpg.de

[†] E-mail: jdexter@mpe.mpg.de

¹ The angular size of Sgr A* is given by $R_s/D \sim 10 \mu\text{as}$, where $R_s \sim 1.36 \times 10^{12}$ cm is the Schwarzschild radius.

tions (Baganoff et al. 2001) of hot gas at the Bondi radius (Agol 2000; Quataert & Gruzinov 2000). At the Bondi accretion rate, the *internal* Faraday rotation within the emitting plasma should depolarize the synchrotron radiation at 230 GHz. Later detections of *external* Faraday rotation allow an estimate of the accretion rate $\sim 10^{-9} - 10^{-7} M_{\odot} \text{ yr}^{-1}$ (Bower et al. 2003; Marrone et al. 2006), a factor ≈ 100 smaller than the Bondi value.

EHT observations provide the opportunity to measure the *spatially resolved polarization*, and show that this fraction can rise to up to 20–40% on event horizon scales (Johnson et al. 2015). They interpret this as evidence for a balance of order and disorder in the underlying polarization map, which can be well matched by maps from GRMHD simulations (Gold et al. 2017).

Here we use polarized radiative transfer calculations of a single snapshot from an axisymmetric GRMHD simulation (§2) to understand how the resulting polarization properties depend on the physical parameters of the emitting plasma. We show that internal Faraday effects become strong in a significant range of model parameter space, scrambling and depolarizing the resulting polarization maps (§3). Measuring the correlation length of the polarization direction from spatially resolved data provides the cleanest way to set limits on the underlying properties of the plasma. We show how this can be measured from future EHT data as a novel constraint on the mass accretion rate and electron temperature of the Sgr A* accretion flow.

2 ACCRETION FLOW AND EMISSION MODELS

We consider a snapshot of a 2D axisymmetric numerical solution (Dexter et al. 2010) from the public version of the GRMHD code HARM (Gammie et al. 2003; Noble et al. 2006), where the initial conditions consist of a rotating black hole with dimensionless spin $a = 0.9375$ surrounded by a torus in hydrostatic equilibrium (Fishbone & Moncrief 1976) threaded with a weak poloidal magnetic field. The system evolves according to the ideal MHD equations in the Kerr spacetime.² Turbulence due to the MRI produces stresses within the torus and leads to an outward transport of angular momentum, causing accretion of material onto the black hole.

Synchrotron radiation is produced by the hot, magnetised plasma and travels through the emitting medium. In the absence of any other effects, the resulting polarization configuration seen by a distant observer traces the magnetic field structure of the gas.³ However, as light travels the polarization angle is rotated both by parallel transport in the curved spacetime near the black hole and by Faraday rotation in the magnetised accretion flow, the latter being

characterised by the Faraday rotation depth, $\tau_{\rho_V} = \int \rho_V dl$, where

$$\rho_V = (e^3 / \pi m_e^2 c^2) \cos \theta_B n_e B f(T_e, \vec{B}) / \nu^2; \quad (1)$$

ρ_V is the Faraday rotation coefficient, e, m_e, n_e are the electron charge, mass and number density respectively, θ_B is the angle between the line of sight and the magnetic field \vec{B} with $|\vec{B}| = B$, c and ν are the light speed and frequency, and $f(T_e, \vec{B})$ is a function of \vec{B} and the electron temperature T_e , but approximately $f \approx T_e^{-2}$ (Jones & Hardee 1979; Quataert & Gruzinov 2000). All quantities are measured in the comoving orthonormal fluid frame (Shcherbakov & Huang 2011; Dexter 2016).

MHD simulations without radiation self-consistently evolve $P_{\text{gas}}/n \sim T_p$ and B^2/n , where P_{gas} is the gas pressure, n and T_p are the proton density and temperature respectively. Choosing the black hole mass sets the length and timescales, while the mass accretion rate \dot{M} is a free parameter which sets the density scale. The electron temperature T_e is not self-consistently computed, and one must make a choice for it. Different approaches have been taken to parametrise T_e , from a constant T_p/T_e within the accretion flow (Mościbrodzka et al. 2009) to directly evolving it with the fluid (Ressler et al. 2015, 2017; Chael et al. 2018) assuming some electron heating prescription (Howes 2010; Rowan et al. 2017; Werner et al. 2018). We assume that $T_e(\eta, \alpha) = \eta T_p/\alpha$, with $\eta \in (0, 1]$ a constant ratio between the electron and proton temperatures and $\alpha = \alpha(\mu, \beta)$ a function that depends on the magnetisation of the plasma similar to the one used in Mościbrodzka et al. (2016):⁴

$$\alpha = \mu \frac{\beta^2}{1 + \beta^2} + \frac{1}{1 + \beta^2}, \quad (2)$$

where the plasma parameter $\beta = P_{\text{gas}}/P_{\text{mag}}$ states the ratio between the gas and magnetic pressures and μ is a free parameter that describes the electron to proton coupling in the weakly magnetised zones (disc body) of the simulation.

The numerical solution we use has a Blandford-Znajek jet (McKinney 2006). Different choices of μ , the electron-proton coupling factor in Eq. 2, can cause the wall between the accretion flow and the jet to shine. When μ in equation 2 is small, the disc has a very high temperature and lights up at 230 GHz due to the fact that, compared to the jet, it has both the highest density and magnetic field strength. However, the larger the μ the colder the disc is and the fainter it gets. If one wishes to maintain a fixed flux, the accretion rate onto the black hole \dot{M} must increase. As a consequence, the jet wall can light up first even given its lower density and field strength.

For a given choice of η and $\mu = (1, 2, 5, 10, 40, 100)$, \dot{M} is then chosen in such a way that the total flux F_V at 230 GHz is either 3 Jy or 0.3 Jy. We chose the first value to model Sgr A* and the second, 0.3 Jy, arbitrarily to decrease α_I/ρ_V , where α_I is the total absorption coefficient. This second option for F_V gives us the opportunity to study models in the optically thin regime to separate the effects of absorption and Faraday rotation.

Given that $n_e \propto \dot{M}$, $B \propto \dot{M}^{1/2}$, $F_V \propto n_e^{\xi} B^{\kappa} T_e^{\sigma}$ (where

⁴ We have taken $\mu = R_{\text{high}}$ and $R_{\text{low}} = 1$ in the (Mościbrodzka et al. 2016) expression.

² Our snapshot is taken at time $t = 2000 GM/c^3$, where G is the gravitational constant, M is the mass of the black hole and c is the light speed.

³ So that the emitted polarization vector is perpendicular to the local magnetic field direction, we use $\text{EVPA} = 1/2 \tan^{-1}(U/Q)$, where EVPA is the electric vector position angle and Q and U are Stokes parameters.

typically $\xi \in [0, 1]$, $\kappa \in [0, 2]$, $\sigma \in [1, 4]$), and assuming a constant F_v , we can express the Faraday rotation depth, $\tau_{\rho v}$, as a function of \dot{M} :

$$\tau_{\rho v} \sim n_e B T_e^{-2} \propto \dot{M}^\delta; \quad (3)$$

where $\delta \equiv 3/2 + (2\xi + \kappa)/\sigma \simeq 3/2 - 7/2$. It can be seen from eq. 3 that $\tau_{\rho v}$ has a strong dependence on \dot{M} and small changes of this quantity reflect as big differences in $\tau_{\rho v}$. Due to this, models with similar physical parameters can vary widely in the strength of the internal Faraday effects and, for $\tau_{\rho v} \gtrsim 1$, in the resulting polarization structure.

To account for emission, absorption, parallel transport and Faraday effects locally within the accretion flow, we employ the publicly available numerical code GRTRANS (Dexter & Agol 2009; Dexter 2016)⁵ to do a self-consistent fully relativistic ray tracing radiative transfer calculation at 230 GHz. The output of the calculation is a polarized image of our GRMHD snapshot as seen by a distant observer at a 50 degree inclination from the black hole (and accretion flow) rotation axis.

3 RESULTS

Fig. 1 shows the resulting intensity-weighted, image-averaged electron temperature $\langle T_e \rangle$, polar angle $\langle \cos \theta \rangle$, and Faraday rotation depth $\langle \tau_{\rho v} \rangle$ for each input model with varying (\dot{M}, T_e) . The steady decrease of $\langle T_e \rangle$ with \dot{M} in the upper left panel of Fig 1 points to “disc-like” systems. The transition to “jet-like” systems happens when the circles show a constant behaviour with \dot{M} and is highly dependent on μ . As discussed before, at large μ the jet has a high enough temperature that it can outshine the cold disc.

This is shown as well in the right panel of Fig. 1, where the cosine of the inclination angle where most of the emission comes from, $\langle \cos \theta \rangle$, as a function of \dot{M} is plotted. It can be seen that at high \dot{M} , models that have the same accretion rate but different μ values have different emission regions. As the electron-proton coupling μ increases, the emission region moves towards the poles indicating a transition to a more “jet-like” system.

In the bottom panel of Fig. 1 we plot the intensity-weighted image-averaged Faraday rotation depth $\langle \tau_{\rho v} \rangle$ vs \dot{M} and the scaling relation in eq. 3, with $\delta = 2$.⁶ This panel shows very nicely the wide spread in $\langle \tau_{\rho v} \rangle$ values as a function of \dot{M} , supporting the idea that systems with similar physical parameters can have widely varying strengths of Faraday rotation. This makes $\langle \tau_{\rho v} \rangle$ a sensitive tracer of the physical conditions of the plasma.

Fig. 2 shows four sample polarized images. Plotted in the background is the total intensity image centred on the black hole (colour shows total flux on a linear scale where the lighter the shade the greater the emission).

These images show the accreting material in characteristic asymmetric crescent shapes: due to Doppler beaming in the rotation torus, the left side where the gas approaches the observer is much brighter than the right side. Furthermore,

strong relativistic light bending lets us see behind the black hole, whose emission appears to be coming from above and below it in the images. In the foreground, white ticks show linear polarization fraction (LP) direction with their length proportional to the LP magnitude (given by $\sqrt{Q^2 + U^2}$). This is what we refer to as a polarization map (PM).

The images shown in Fig. 2 have a variety of model parameters. In the upper left panel an optically thick image is shown. In this case, the system resembles a black body, dominated by optical absorption and is completely depolarized from self-absorption. We can see a case of the Blandford-Znajek jet wall lighting up in the upper right panel of Fig. 2 for a case where $\mu = 100$.

The bottom panels of Fig 2 are optically thin. In the case of weak Faraday effects (hot, tenuous emitting medium - high T_e and low \dot{M} , $\langle \tau_{\rho v} \rangle < 1$; bottom left panel), the polarization traces the toroidal magnetic field (horizontal where the light comes from the approaching gas and vertical where it comes from gas behind the black hole) and displays an ordered behaviour (due to the axisymmetry of the system). The combination of this with the crescent shape background image leads to such a characteristic polarization map (Bromley et al. 2001). When considering the polarization over the whole image, the contributions from each of the vector components may cancel, resulting in a lower LP over the image (*beam depolarization*). Strong Faraday effects (colder, denser medium - low T_e , high \dot{M} ; bottom right panel of Fig. 2) can scramble and depolarize the image on small scales.

3.1 Linear Polarization Fraction and Rotation Measure in the models.

Fig. 3 shows the net intensity-weighted LP integrated over the image versus the intensity-weighted image-averaged Faraday rotation depth, $\langle \tau_{\rho v} \rangle$. The images generally depolarize with increasing $\langle \tau_{\rho v} \rangle$, as expected. However, the individual behaviour between both sets of models (diamonds and circles) is different, and no smooth or uniform LP trend as a function of $\langle \tau_{\rho v} \rangle$ can be extracted.

Given a measurement of LP, one could use Fig. 3 to set an upper limit on $\langle \tau_{\rho v} \rangle$ and obtain the models that satisfy the restriction set by the LP. As an example, a variety of our “disc-like” models where $\langle \tau_{\rho v} \rangle$ varies over many orders of magnitude ($\sim 5 \times 10^{-2} - 1 \times 10^2$) satisfy the measured 5–10% LP for Sgr A* at 230 GHz (Aitken et al. 2000). The emission is locally strongly polarized ($\gtrsim 40\%$) but is naturally beam depolarized due to the combination of the crescent image and toroidal magnetic field configuration. The “jet-like” models ($\langle \tau_{\rho v} \rangle \gtrsim 10^2$) on the other hand are heavily depolarized, and cannot match the observed LP of Sgr A*.

We looked at the dependence of the rotation measure (RM) of the images with $\langle \tau_{\rho v} \rangle$ as well and found, as expected, that the RM increases with $\langle \tau_{\rho v} \rangle$. However, we could not get a clean measurement like in Bower et al. (2003) and Marrone et al. (2006) because our simulation domain is not as large as that in their work. We can look at this in the future, but it would require very long duration simulations (e.g., Narayan et al. 2012) to reach inflow equilibrium at the large radii of the external Faraday screen.

⁵ <http://www.github.com/jadexter/grtrans>

⁶ We included the effects of Faraday conversion in the radiative transfer calculation as well, but it is significantly weaker than Faraday rotation, and so we focus our study to the latter.

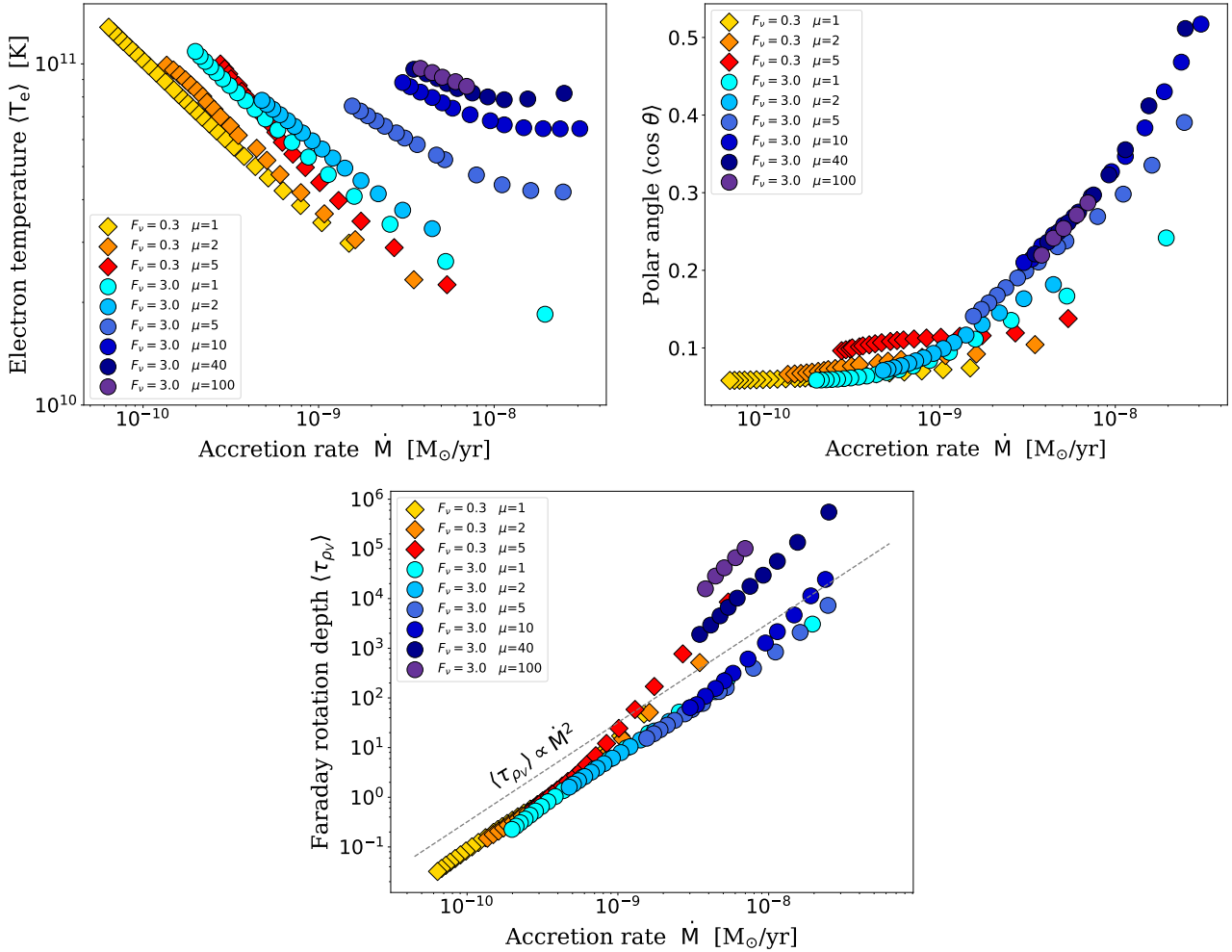


Figure 1. Intensity-weighted, image-integrated model quantities. Each dot is a chosen (\dot{M}, T_e) pair with F_ν indicated by a colour scale: diamonds for $F_\nu = 0.3$ Jy and circles for $F_\nu = 3$ Jy. The colour gradient shows the choice for μ , where the lighter (darker) the shade, the lower (higher) the μ value is. **Upper left:** Intensity-weighted, image-averaged electron temperature $\langle T_e \rangle$ vs \dot{M} . The models that show a steady decrease of $\langle T_e \rangle$ with \dot{M} are more “disc-like” systems. The transition to “jet-like” systems happens where the decrement stops and becomes constant with \dot{M} . **Upper right:** Intensity-weighted image-averaged emission angle $\langle \cos \theta \rangle$ as a function of \dot{M} . At high \dot{M} , as μ increases the emission region moves towards the poles, indicating the transition to a more “jet-like” system. **Bottom:** Intensity-weighted image-averaged Faraday rotation depth $\langle \tau_{\rho_V} \rangle$ vs \dot{M} . It can be seen how $\langle \tau_{\rho_V} \rangle$ extends over a wide range of values with \dot{M} . A scaling relation between both quantities is shown with a dotted line where $\delta = 2$.

3.2 The Correlation Length.

The upper panels of Fig 2 can be easily distinguished from their total intensity images alone and might be disfavoured already from the measured size of the source and spectral observations. In the optically thin regimes however (bottom panels), the total intensity images are hard to tell apart and are generally consistent with the observational constraints (Mościbrodzka et al. 2009; Dexter et al. 2010). The polarization maps however, vary substantially. This spatial configuration of the polarization offers an alternative to learning about the physical parameters of the models.

To characterise the degree of order of each map produced by a particular (\dot{M}, T_e) pair, we use a quantity which we call the “correlation length”, λ . Large values of λ point to an ordered configuration, limited by the coherence of the magnetic field structure, whereas small values indicate a more disordered configuration.

To calculate this quantity we autocorrelate each map. Because the PM is a vector field, we look at each component separately and weight their value at each pixel by Stokes I at the same pixel⁷ (left panel of Fig. 4). The result is a 2D function that gives information on how the polarization component varies spatially. We then take 50 “1D slices” of this function in different angular directions to account for the spatial changes in 2D and take the average of their widths at 0.5 (FWHM, middle and right panels of Fig. 4). Twice this value is the polarized correlation length in μ as.

Figure 5 shows the correlation length (λ_x and λ_y , x and y subindices for each vector component) of each simulation’s

⁷ The reference system is orthonormal with one of the axes aligned with the spin axis of the black hole and the other in a direction perpendicular to the observer (Bardeen et al. 1972).

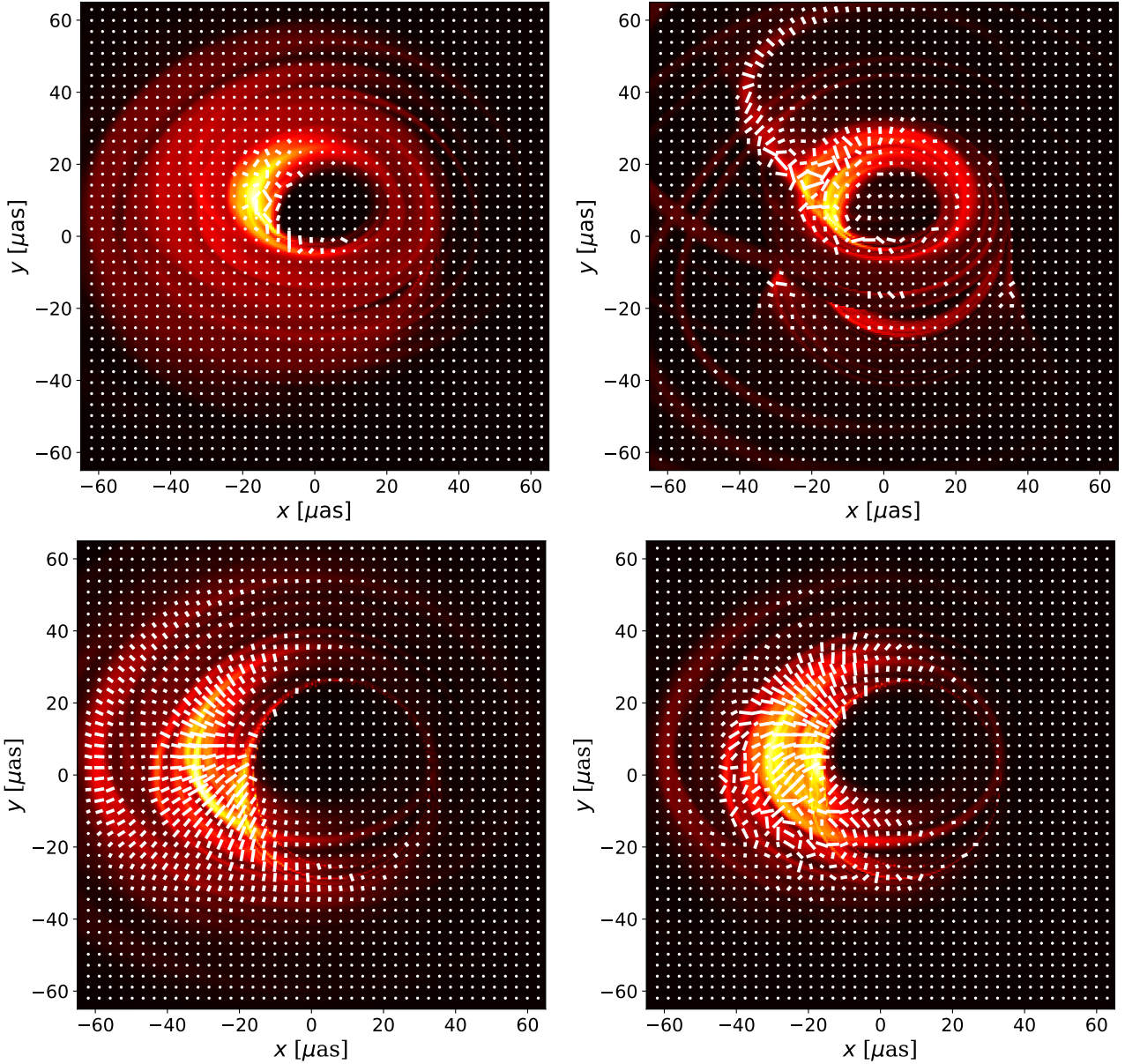


Figure 2. Polarization maps obtained from different μ and (\dot{M}, T_e) pairs. It can be seen how the Faraday effects affect the polarization. **Upper left panel:** optically thick image. The accretion flow emits like a blackbody and is depolarized. **Upper right panel:** depending on the choice for the electron to proton coupling, the wall between the Blandford-Znajek jet and the accretion flow may become apparent. **Bottom left panel:** weak Faraday effects. The ticks trace the smooth magnetic field configuration. **Bottom right panel:** strong Faraday effects. The ticks are disordered and the underlying magnetic field structure is less evident.

PM as a function of the intensity-weighted image-averaged Faraday rotation depth $\langle\tau_{\rho_V}\rangle$.

The overall behaviour of the correlation length for both components is as expected. At small $\langle\tau_{\rho_V}\rangle$ (small \dot{M} , large T_e), the Faraday effects are weak implying coherent PMs in which the changes are given by the geometry of the magnetic field in the gas, resulting in a maximum of the correlation length. As $\langle\tau_{\rho_V}\rangle$ increases, the Faraday effects become stronger, the scrambling becomes more apparent and the correlation length decreases, showing a sharp drop at around $\langle\tau_{\rho_V}\rangle \approx 1$. In the case of the correlation length for the x component, there is a small increase after the minimum that remains until high values for $\langle\tau_{\rho_V}\rangle$ which we associate

with the internal structure of the polarization. This does not appear in the λ_y plot.

Unlike the LP (Fig. 3), the 0.3 Jy and 3 Jy correlation length curves have the same shape and eventually overlap, which points towards a universal behaviour for this quantity (in the limited range of models studied so far). This has powerful implications, since measuring λ sets a model-independent upper limit on $\langle\tau_{\rho_V}\rangle(\dot{M}, T_e, \beta, H/R)$, where H/R is the scale height of the disc.

One can relate the correlation length directly to observable quantities in VLBI (Johnson et al. 2015). In their paper, Johnson et al. (2015) show examples with Gaussian intensity distributions and constant net LP (6–7%), and a varying

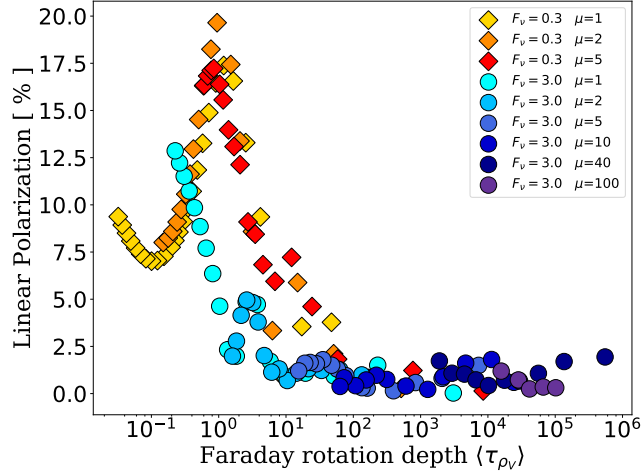


Figure 3. Net linear polarization fraction plotted against the intensity-weighted image-averaged Faraday rotation depth $\langle \tau_{\rho_V} \rangle$. The same colour and marker criteria has been used as that in figure Fig. 1. As the Faraday effects become stronger, the LP decreases, as expected. However the behaviour is neither smooth nor universal ($\langle \tau_{\rho_V} \rangle \lesssim 10^2$). “Jet-like” models have high Faraday optical depths ($\langle \tau_{\rho_V} \rangle \gtrsim 10^2$) from the cold, dense disc and are heavily depolarized, failing to reproduce the Sgr A* LP of $\approx 5 - 10\%$.

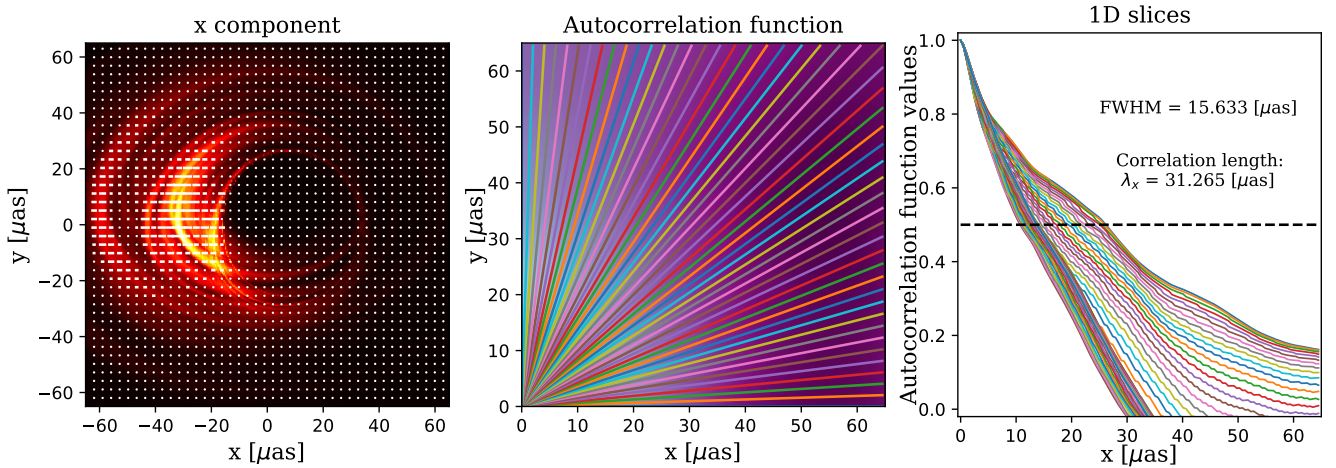


Figure 4. Illustration of the calculation of the polarized correlation length. **Left:** take one of the vector components of the polarization (x component shown here) and auto-correlate the map. **Middle:** Plotted in the background in shades of purple is the 2D autocorrelation function. We take 1D slices of this function in different angular directions (coloured solid lines in the foreground) to account for the 2D behaviour. **Right:** 1D slices from the autocorrelation function. Twice the average of their values at 0.5 (FWHM) is how we define as the polarized correlation length, λ_x , in μas .

polarization structure with a prescribed coherence length. They find a correlation length of 0.29 times the Gaussian FWHM of the model. Measuring an approximate Gaussian FWHM for our images and multiplying it by 0.29 gives us an estimated correlation length of $11.6\mu\text{as}$. We then use Fig. 5 to set an upper limit on the $\langle \tau_{\rho_V} \rangle \lesssim 1$, in agreement with the qualitative argument of Agol (2000) and Quataert & Gruzinov (2000). However, our models are not Gaussians and it is not clear that the λ value inferred by Johnson et al. (2015) applies here.

We can extend the analysis further into visibility space. Fig. 6 shows the Stokes parameters I , Q and U (top) and their respective visibilities \tilde{I} , \tilde{Q} and \tilde{U} (bottom) of one of

our simulations. On large scales, it can be seen that Q and U resemble I , showing the same crescent structure. However, on smaller scales some deviation becomes evident because the polarization, \vec{p} , is changing. Therefore, on the largest scales one gets information on I and on the smallest scales one sees the polarization properties.

If we study this in the visibility space uv and take the Fourier Transform (FT) of the Stokes parameters (bottom images of Fig. 6), the roles are inverted. Large scale features become small and vice versa. In this respect, the shape of the total intensity image becomes a small “beam” in uv , whereas the large scale structure observed in the \tilde{Q} and \tilde{U} images

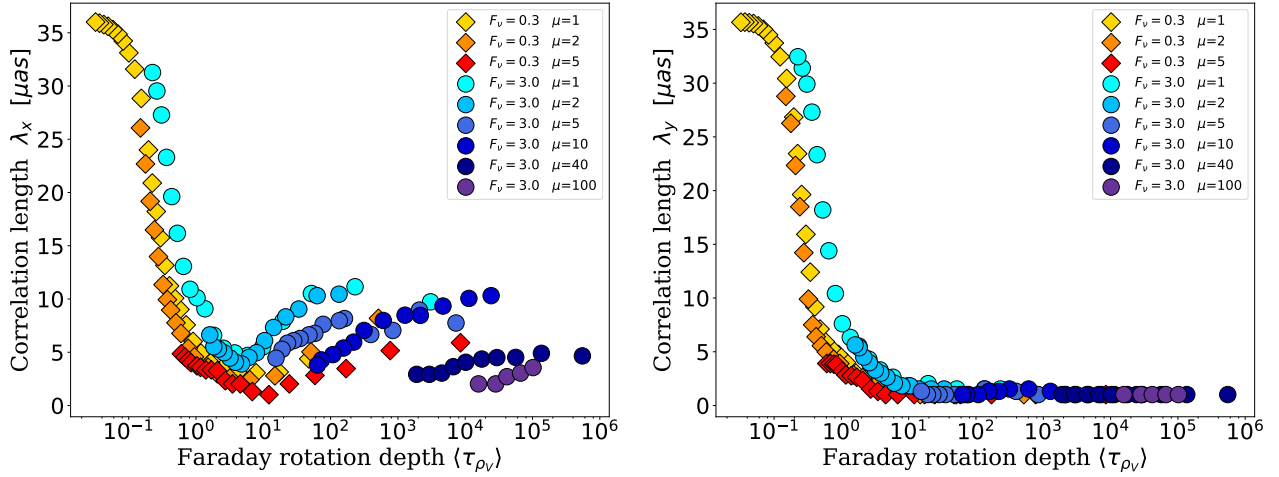


Figure 5. Correlation length measured for x and y vector components (left and right panels respectively) of PMs with different μ and (M, T_e) values plotted against the intensity-weighted image-averaged Faraday rotation depth $\langle \tau_{\rho_V} \rangle$. The same colour and marker criteria is used as that in Fig. 1 and Fig. 3. Coherent maps are obtained when $\langle \tau_{\rho_V} \rangle \lesssim 1$ and scrambling appears as the Faraday effects become stronger. A measurement of the correlation length places a model-independent upper limit on $\langle \tau_{\rho_V} \rangle$, and in turn the lower limits on the plasma electron temperature and relative magnetic field strength.

corresponds to the smallest angular scales in Q and U and reflects the properties of the polarization map.

One can think of the images as the convolution of I with \vec{p} , with the result interpreted as I being smeared out by \vec{p} with some characteristic scale that reflects the inner structure of the latter. In the case of a completely disordered polarization map, taking the FT of the image would give what would basically be a noise map in the visibility space, with no characteristic scale at which the polarization's behaviour stands out. On the other hand, the FT of the convolution between I and a completely ordered \vec{p} would give an image with a nice beam centred at $uv = 0$ and no noise whatsoever.

We are interested in finding the characteristic scale at which the random fluctuations or noise in the polarization is suppressed. We call this the polarized correlation length of the visibility, $\lambda_{\vec{p}}$, where x is one of the Stokes parameters.

We measure this as the uv distance at which the visibility's amplitude drops permanently below a certain value. As an example, we have chosen this quantity to be 10% of \tilde{Q}_{\max} and \tilde{U}_{\max} , where \tilde{Q}_{\max} and \tilde{U}_{\max} are the maximum visibility amplitudes. We define the visibility correlation length as the inverse of the averaged distances which satisfy this criteria. The calculated $\lambda_{\vec{Q}}$ and $\lambda_{\vec{U}}$ for our models are shown in Fig. 7.

As shown in Fig. 7, the correlation length measured in the visibility space can also constrain $\langle \tau_{\rho_V} \rangle$ and is measured directly from VLBI observables. With upcoming data from the EHT, this quantity may be promising for inferring the characteristics of the plasma in the system.

4 DISCUSSION

Sgr A* is a great laboratory for testing accretion physics and general relativity. Polarization is a powerful tool for determining the plasma properties and the magnetic field structure.

From a GRMHD simulation of a torus of magnetised plasma in initial hydrostatic equilibrium with a poloidal magnetic field, we have done self-consistent fully relativistic ray tracing radiative transfer calculations of the radiation at 230 GHz. We have analysed the different polarized images and characterised the degree of coherence in the polarization map as a function of the Faraday rotation depth. This coherence scale we call the correlation length. Large values of this quantity are expected when the Faraday effects are weak and the maps are ordered. Small values of the correlation length in our models point to large Faraday rotation depth values and disordered maps.

We have proposed a method to relate the polarized correlation length calculated from the images to direct observables of VLBI by taking the Fourier Transform of the images and analysing the large scale structure of the visibilities in the Fourier domain. This shows a similar behaviour to that showed in the image space, with the advantage that it uses VLBI observables.

In the past, unresolved polarization of Sgr A* has been very helpful in constraining models. With the new EHT measurements this can be done with the polarization map itself for the first time through the correlation length. So far, the behaviour of this new quantity appears to be model independent, which makes it a promising approach that can be used to set restrictions on the plasma parameters around the black hole and distinguish models robustly in a way that is often difficult with total intensity images alone.

Constraining $\langle \tau_{\rho_V} \rangle \sim n_e B T_e^{-2}$ places limits on the physical properties of the accreting gas, most directly T_e . In addition, $B^2 \sim \beta^{-1} n T_p$. From hydrostatic equilibrium, $T_p \sim T_{\text{vir}} (H/R)^2$, where $T_{\text{vir}} \sim m_p c^2 / r$ is the virial temperature at dimensionless radius $r = R/R_s$ and H/R is the scale height of the accretion flow. The relative field strength then scales as $B^2/n \sim \beta^{-1} (H/R)^2$. At fixed flux density, a limit on $\langle \tau_{\rho_V} \rangle$

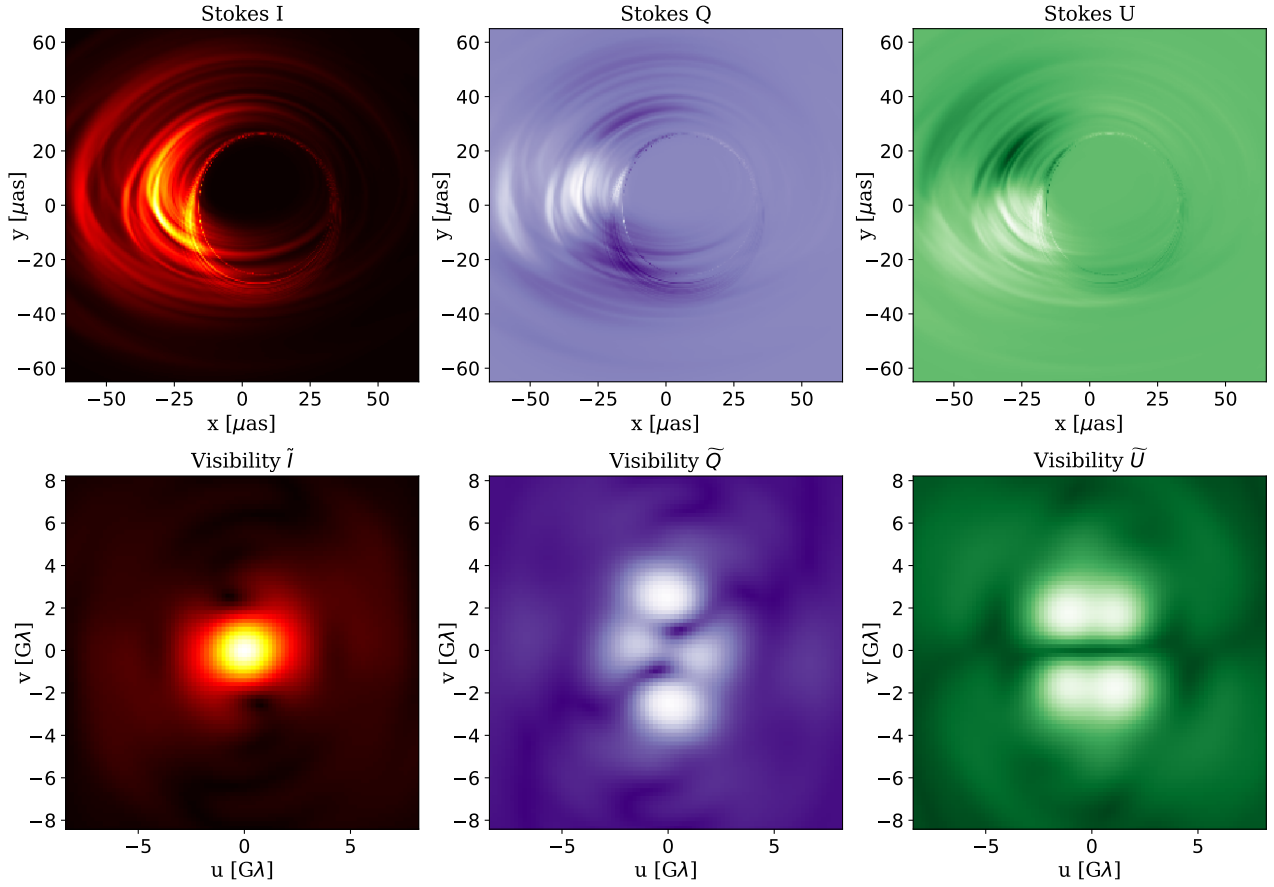


Figure 6. I , Q and U Stokes parameters for one of our simulations in image (top panels) and visibility space (bottom panels). On the top images, it can be seen that Q and U resemble I on large scales, with different substructure due to the changing polarization. On the visibility space however (bottom panels), small scale features in \tilde{Q} and \tilde{U} give information on I whereas the large scale structure corresponds to the polarization.

constrains a combination of the magnetic field strength and disc scale height as well as the electron temperature.

We have only considered one inclination. We expect that the trend of decreasing LP and correlation length with increasing Faraday rotation optical depth holds at all viewing geometries, but their maximum values at low Faraday rotation depth will be model-dependent.

We have also neglected the effects of interstellar scattering. The diffusive part of the scattering should not affect the correlation length results, since we use ratios of the Stokes parameters which are all modified in the same way. The refractive part of the scattering (e.g., Gwinn et al. 2014) could in particular complicate our proposed method for measuring the correlation length in the Fourier domain, since it will introduce signal beyond that corresponding to small scale structure in the polarization map.

We have demonstrated the technique with a single snapshot from an axisymmetric GRMHD simulation. This has some limitations given that the MRI is unsustainable in 2D and the simulation can only be studied for short times. Therefore, the degree of order seen for $\langle \tau_{\rho v} \rangle < 1$ (bottom left panel of Fig. 2) is somewhat overestimated compared to 3D

simulations. Extensions to 3D and studying time variability are goals for future work. The time variable polarized correlation length could for example be used to measure the properties of MRI turbulence in EHT data.

We have focused here on the case of mm-VLBI of Sgr A*, but the same technique should apply to M87 (Mościbrodzka et al. 2017) or any other synchrotron source with a resolved polarization map. In particular, in polarized VLBI images of radio jets past work has focused on measuring the Faraday rotation across the image (e.g., Zavala & Taylor 2003; O’Sullivan et al. 2018). Here we have shown that the correlation length may be a more robust indicator of the Faraday optical depth, if there is a significant contribution from within the emission region.

ACKNOWLEDGEMENTS

The authors thank M. Johnson, M. Mościbrodzka, C. Gammie, A. Broderick, R. Gold, J. Kim, and D. P. Marrone for useful discussions related to Sgr A* polarization and radiative transfer. This work was supported by a CONA-

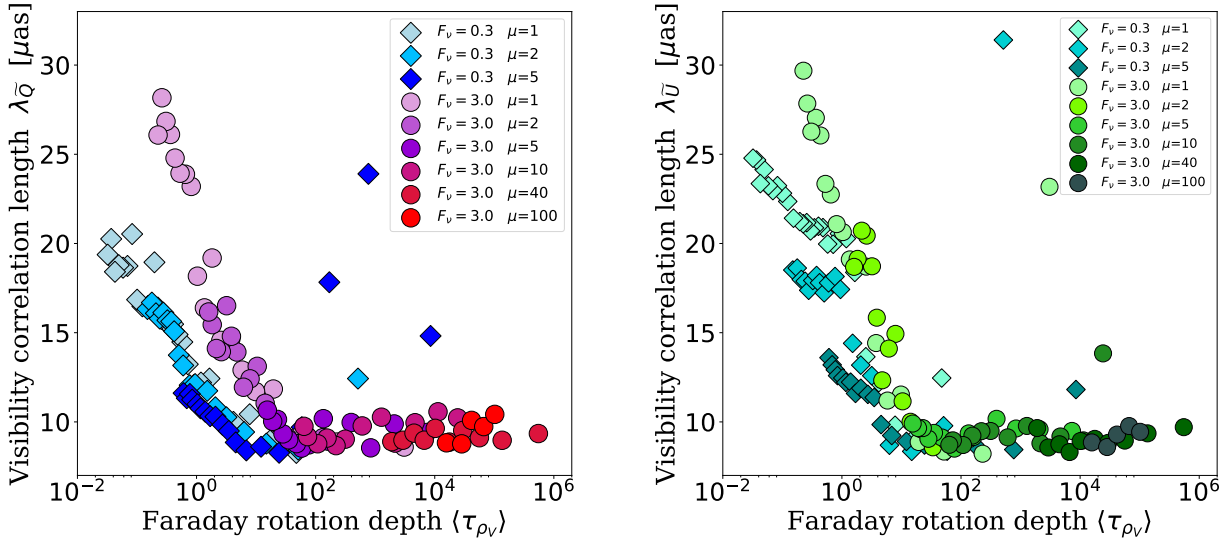


Figure 7. Polarized correlation length in the Fourier domain using \bar{Q} (left panel) and \bar{U} (right panel) for our models. The criteria used was to take the inverse of the averaged uv distances at which the amplitude of the visibility drops below 10% of each respective visibility maximum, \bar{Q}_{\max} and \bar{U}_{\max} for each model. As in the image domain, the correlation length drops sharply for $\langle \tau_{\rho\nu} \rangle \gtrsim 1$.

CyT/DAAD grant (57265507) and by a Sofja Kovalevskaja award from the Alexander von Humboldt foundation.

REFERENCES

- Agol E., 2000, *ApJ*, **538**, L121
- Aitken D. K., Greaves J., Chrysostomou A., Jenness T., Holland W., Hough J. H., Pierce-Price D., Richer J., 2000, *ApJ*, **534**, L173
- Baganoff F. K., et al., 2001, *Nature*, **413**, 45
- Balbus S. A., Hawley J. F., 1991, *ApJ*, **376**, 214
- Bardeen J. M., Press W. H., Teukolsky S. A., 1972, *ApJ*, **178**, 347
- Boehle A., et al., 2016, *ApJ*, **830**, 17
- Bower G. C., Wright M. C. H., Falcke H., Backer D. C., 2003, *ApJ*, **588**, 331
- Bower G. C., et al., 2015, *ApJ*, **802**, 69
- Broderick A. E., Loeb A., 2006, *MNRAS*, **367**, 905
- Broderick A. E., Fish V. L., Doeleman S. S., Loeb A., 2011, *ApJ*, **735**, 110
- Bromley B. C., Melia F., Liu S., 2001, *ApJ*, **555**, L83
- Chael A., Rowan M. E., Narayan R., Johnson M. D., Sironi L., 2018, preprint, ([arXiv:1804.06416](https://arxiv.org/abs/1804.06416))
- Chan C.-K., Psaltis D., Özel F., Narayan R., Sądowski A., 2015, *ApJ*, **799**, 1
- Dexter J., 2016, *MNRAS*, **462**, 115
- Dexter J., Agol E., 2009, *ApJ*, **696**, 1616
- Dexter J., Agol E., Fragile P. C., McKinney J. C., 2010, *ApJ*, **717**, 1092
- Doeleman S. S., et al., 2008, *Nature*, **455**, 78
- Falcke H., Markoff S., 2000, *A&A*, **362**, 113
- Falcke H., Markoff S. B., 2013, *Classical and Quantum Gravity*, **30**, 244003
- Fish V. L., et al., 2011, *ApJ*, **727**, L36
- Fishbone L. G., Moncrief V., 1976, *ApJ*, **207**, 962
- Gammie C. F., McKinney J. C., Tóth G., 2003, *ApJ*, **589**, 444
- Genzel R., Eisenhauer F., Gillessen S., 2010, *Reviews of Modern Physics*, **82**, 3121
- Gillessen S., et al., 2017, *ApJ*, **837**, 30
- Gold R., McKinney J. C., Johnson M. D., Doeleman S. S., 2017, *ApJ*, **837**, 180
- Gwinn C. R., Kovalev Y. Y., Johnson M. D., Soglasnov V. A., 2014, *ApJ*, **794**, L14
- Howes G. G., 2010, *MNRAS*, **409**, L104
- Johnson M. D., et al., 2015, *Science*, **350**, 1242
- Jones T. W., Hardee P. E., 1979, *ApJ*, **228**, 268
- Kamruddin A. B., Dexter J., 2013, *MNRAS*, **434**, 765
- Marrone D. P., Moran J. M., Zhao J.-H., Rao R., 2006, *ApJ*, **640**, 308
- McKinney J. C., 2006, *MNRAS*, **368**, 1561
- Mościbrodzka M., Gammie C. F., Dolence J. C., Shiokawa H., Leung P. K., 2009, *ApJ*, **706**, 497
- Mościbrodzka M., Falcke H., Shiokawa H., Gammie C. F., 2014, *A&A*, **570**, A7
- Mościbrodzka M., Falcke H., Shiokawa H., 2016, *A&A*, **586**, A38
- Mościbrodzka M., Dexter J., Davelaar J., Falcke H., 2017, *MNRAS*, **468**, 2214
- Narayan R., Yi I., 1995, *ApJ*, **452**, 710
- Narayan R., Sądowski A., Penna R. F., Kulkarni A. K., 2012, *MNRAS*, **426**, 3241
- Noble S. C., Gammie C. F., McKinney J. C., Del Zanna L., 2006, *ApJ*, **641**, 626
- O’Sullivan S. P., Lenc E., Anderson C. S., Gaensler B. M., Murphy T., 2018, *MNRAS*, **475**, 4263
- Quataert E., Gruzinov A., 2000, *ApJ*, **545**, 842
- Quataert E., Narayan R., 1999, *ApJ*, **516**, 399
- Ressler S. M., Tchekhovskoy A., Quataert E., Chandra M., Gammie C. F., 2015, *MNRAS*, **454**, 1848
- Ressler S. M., Tchekhovskoy A., Quataert E., Gammie C. F., 2017, *MNRAS*, **467**, 3604
- Rowan M. E., Sironi L., Narayan R., 2017, *ApJ*, **850**, 29
- Shcherbakov R. V., Huang L., 2011, *MNRAS*, **410**, 1052
- Werner G. R., Uzdensky D. A., Begelman M. C., Cerutti B., Nalewajko K., 2018, *MNRAS*, **473**, 4840
- Yuan F., Markoff S., Falcke H., 2002, *A&A*, **383**, 854
- Yuan F., Quataert E., Narayan R., 2003, *ApJ*, **598**, 301
- Zavala R. T., Taylor G. B., 2003, *ApJ*, **589**, 126